Computers and Fluids 121 (2015) 133–144

Contents lists available at ScienceDirect

Computers and Fluids

journal homepage: www.elsevier.com/locate/compfluid

Optimal suppression of flow perturbations using boundary control

Xuerui Mao [a,b,*], Hugh Blackburn [b], Spencer Sherwin [c]

[a] School of Engineering and Computing Sciences, Durham University, Durham DH1 3LE, UK
[b] Department of Mechanical and Aerospace Engineering, Monash University, 3800, Australia
[c] Department of Aeronautics, Imperial College London, South Kensington SW7 2AZ, UK

ARTICLE INFO

Article history:
Received 16 November 2014
Revised 22 June 2015
Accepted 14 August 2015
Available online 24 August 2015

Keywords:
Optimal boundary perturbation
Transient energy growth
Open-loop flow control
Controllability
Stenotic flow
Batchelor vortex

ABSTRACT

Boundary perturbations are considered as flow control forcing and their distributions are optimised to suppress transient energy growth induced by the most energetic disturbances in the domain. For a given control cost (square integration of the control forcing), the optimal control calculated from the proposed optimisation algorithm is proved to be unique. For small values of control cost, a sensitivity solution is obtained and its distribution indicates the sensitivity of perturbation energy on boundary control. For larger control cost, the distribution of the optimal control approaches the stablest mode of a direct-adjoint operator and tends to be grid-to-grid oscillatory. A controllability analysis is further conducted to identify the uncontrollable component of perturbations in the domain. This work underpins the recently thriving linear feed-back flow control investigations, most of which use empirically distributed control actuators, in terms of choosing the location and magnitude of the control forcing and evaluating the maximum control effect. Two case studies are conducted to demonstrate the proposed algorithm; in a stenotic flow, the optimised wall boundary control is observed to suppress over 95% of the transient energy growth induced by the global optimal initial perturbation; in the Batchelor vortex flow, the optimal inflow control can effectively suppress the spiral vortex breakdown induced by the development of initial perturbations.

1. Introduction

Perturbations to a base fluid flow can be classified into three broad categories: initial perturbation, external forcing and boundary perturbation, which can be modelled as the initial condition, body force and boundary condition of the linearised Navier–Stokes (NS) equations, respectively, provided that the magnitude of the perturbation is small enough. The calculation of the most energetic distribution of these perturbations has been extensively studied in both local and global frameworks [1–5].

The initial perturbations can be in the form of random perturbations, most unstable eigenmodes or optimal initial perturbations. The fluid dynamics community have devoted much effort to calculating the most unstable mode in asymptotically unstable flows or the optimal initial perturbation in stable/weakly unstable flows. In unstable flows the evolution operator for initial perturbations has eigenvalues with positive real parts corresponding to unstable eigenmodes (grow in magnitude with time). For stable/weakly unstable flows, where all the eigenmodes may decay in the large-time limit, non-normality of the evolution operator for initial perturbations produces optimal perturbations which can be expanded as a linear combination of the stable eigenmodes and exhibit transient energy growth before eventually decaying. The optimal initial perturbation and its associated energy growth can be obtained through singular value decomposition of the evolution operator or eigenvalue decomposition of a direct-adjoint operator [4,6,7].

For flow behaving as an "amplifier", which is globally stable but has locally unstable regions, an initial perturbation study does not capture the full dynamics—even though transient energy growth can be observed as the perturbation passes the unstable region, the flow returns to the unperturbed state after the perturbation is convected out of the domain. To these perturbation "amplifiers", a temporally continuous perturbation is required to keep the unstable region perturbed and model effects of ubiquitously existing noise. Both boundary perturbations and external forcing can be used to continuously perturb the flow [8,9]. The optimal external forcing can be obtained by singular value decomposition of the resolvent [1,10] and the optimal boundary perturbation can be obtained by singular value decomposition of the evolution operator, eigenvalue decomposition of the direct-adjoint operator or optimisation of the final perturbation energy [11].

The counterpart of calculating the most energetic perturbation and its outcome is to control or suppress the development of perturbations. Such a suppression can be achieved by modifying the

* Corresponding author. Tel.: +4401913342515.
E-mail address: xuerui.mao@durham.ac.uk (X. Mao).

http://dx.doi.org/10.1016/j.compfluid.2015.08.018
0045-7930/

base flow profile to be less sensitive to perturbations, or introducing control whose development cancels the objective perturbation [12–14]. The suppression of perturbation growth, e.g. transient energy growth induced by the optimal initial perturbation, can be achieved by means of boundary control. Such control investigations involve the interaction of at least two types of perturbations: an initial perturbation (and its outcome) in the domain as the control objective and the boundary perturbation as the control variable. To control the growth of a given perturbation, e.g. the optimal initial perturbation, an open-loop control algorithm has been developed in a local framework, where the spatial variation of the control perturbation is fixed and the time sequence is calculated [15]. To control developments of unknown perturbations, linear feed-back control based on reduced-order modelling has received considerable attention most recently to control instabilities or transient responses in asymptotically unstable flow and convectively unstable flow respectively [16–19]. Most of these feed-back control investigations focus on the temporal variation of the control signal produced by actuators whose spatial locations are determined empirically.

In the present work, we concentrate on the spatial location of the boundary control, which is optimised to minimise the energy of perturbations stemming from any of the types of perturbations discussed above. Adopting the optimal initial perturbation and its outcome as the control objective, the computed optimal boundary control indicates the sensitivity of the most energetic component of a random noise to the control and therefore can be used to choose locations of actuators and magnitude of the control forcing in feed-back control studies. A controllability analysis is further conducted by relaxing the constraint on control cost, to predict the uncontrollable component of the objective perturbation.

We then demonstrate the proposed algorithms in two case studies. A wall bounded stenotic flow is adopted as the first example and the wall-normal boundary perturbations are optimised to suppress transient energy growth of the global optimal initial perturbation. Then the Batchelor vortex flow is considered as the second example, and the inflow control is optimised to suppress spiral vortex breakdown induced by the development of initial perturbations.

2. Optimisation methodology

2.1. Governing equations

Starting from the incompressible NS equations

$$\partial_t \boldsymbol{U} = -\boldsymbol{U}\cdot\nabla\boldsymbol{U} - \nabla P + Re^{-1}\nabla^2\boldsymbol{U}, \quad \text{with} \quad \nabla\cdot\boldsymbol{U} = 0,$$

where P is the modified or kinematic pressure, $\boldsymbol{U}$ is the velocity vector and Re is the Reynolds number; the flow field can be decomposed as the sum of a base flow and a perturbation i.e. $(\boldsymbol{U}, P) = (\bar{\boldsymbol{u}}, \bar{p}) + (\boldsymbol{u}, p)$. Then the evolution of small perturbations is governed by the linearised NS (LNS) equations

$$\partial_t \boldsymbol{u} = -\bar{\boldsymbol{u}}\cdot\nabla\boldsymbol{u} - (\nabla\bar{\boldsymbol{u}})^T\cdot\boldsymbol{u} - \nabla p + Re^{-1}\nabla^2\boldsymbol{u}, \quad \text{with} \quad \nabla\cdot\boldsymbol{u} = 0. \tag{1}$$

As (1) is linear, one can further decompose the perturbation field into spanwise Fourier modes in Cartesian coordinates or azimuthal Fourier modes in cylindrical coordinates, each of which will evolve independently, provided that the base flow is homogeneous in the spanwise or azimuthal direction. In the following, we will typically be dealing with $(\boldsymbol{u}, p)_m$, with m denoting the spanwise/azimuthal wave number. To keep notations reasonably compact we implicitly adopt Fourier decomposition for the perturbation field, and only introduce its spanwise/azimuthal Fourier mode index m when required.

2.2. Definition of operators

For clarification, we firstly introduce scalar products

$$(\boldsymbol{a}, \boldsymbol{b}) = \int_\Omega \boldsymbol{a}\cdot\boldsymbol{b}\,\mathrm{d}V \quad \text{and} \quad [\boldsymbol{e}, \boldsymbol{f}] = \int_{\partial\Omega} \boldsymbol{e}\cdot\boldsymbol{f}\,\mathrm{d}S,$$

where $\boldsymbol{a}$ and $\boldsymbol{b}$ are defined on the spatial domain Ω, $\boldsymbol{e}$ and $\boldsymbol{f}$ are defined on the "control boundary" $\partial\Omega$, which refers to the segment of the boundary where the control perturbation is introduced, and τ is a final time.

On the control boundary, a boundary-normal Dirichlet-type condition, denoted as $\boldsymbol{u}_c(\boldsymbol{x}, t)$, is imposed. Here $\boldsymbol{x}$ represents the spatial coordinates on the control boundary. To reduce the dimension of $\boldsymbol{u}_c(\boldsymbol{x}, t)$ after temporal-spatial discretisation, we decompose the temporal and spatial dependence as

$$\boldsymbol{u}_c(\boldsymbol{x}, t) = \boldsymbol{c}(\boldsymbol{x}) f(t, \omega), \quad \text{with} \quad 0 \le t \le \tau, \quad \text{and} \quad \boldsymbol{x} \in \partial\Omega \tag{2}$$

where $\boldsymbol{c}(\boldsymbol{x})$ is the spatial dependence to be optimised and $f(t, \omega)$ is a prescribed temporal dependence function in which ω is a circular frequency [9,11]. The choice of $f(t, \omega)$ will be discussed in detail in the following case studies. We note that the magnitude of the control can be evaluated by the integration of the spatial dependence, i.e. $E_c = [\boldsymbol{c}, \boldsymbol{c}]$, which can be interpreted as the control cost.

To describe the development of the boundary perturbation, we define an evolution operator $\mathcal{N}$ satisfying

$$\boldsymbol{u}_{c\tau} = \mathcal{N}\boldsymbol{c},$$

where $\boldsymbol{u}_{c\tau}$ is the velocity vector of the response flow field to the boundary perturbation at time τ. This operator corresponds to the integration of (1) with initial condition $\boldsymbol{u}|_{t=0} = 0$ and boundary condition as specified in (2) on the control boundary.

Similar as discussed in [9], A dual operator of $\mathcal{N}$ is defined such that

$$(\mathcal{N}\boldsymbol{c}, \boldsymbol{b}) = [\boldsymbol{c}, \mathcal{N}^*\boldsymbol{b}]. \tag{3}$$

Clearly this dual operator projects a velocity vector defined on the computational domain to a vector defined on the control boundary. The action of this dual operator on a velocity vector $\boldsymbol{u}_\tau^*$ can be calculated as

$$\mathcal{N}^*\boldsymbol{u}_\tau^* = \boldsymbol{n}\cdot\int_0^\tau (p^*\boldsymbol{n} - Re^{-1}\nabla_{\boldsymbol{n}}\boldsymbol{u}^*) f^*(t, \omega)\,\mathrm{d}t, \tag{4}$$

where $\boldsymbol{n}$ is a unit outward normal on the control boundary, $f^*(t, \omega)$ is the adjoint operator of $f(t, \omega)$ satisfying $[f(t, \omega)\boldsymbol{c}, \boldsymbol{e}] = [\boldsymbol{c}, f^*(t, \omega)\boldsymbol{e}]$, and p^* and $\boldsymbol{u}^*$ are adjoint velocity and adjoint pressure, respectively. The adjoint variables are obtained by integrating the adjoint equations

$$-\partial_t\boldsymbol{u}^* = \bar{\boldsymbol{u}}\cdot\nabla\boldsymbol{u}^* - \nabla\bar{\boldsymbol{u}}\cdot\boldsymbol{u}^* - \nabla p^* + Re^{-1}\nabla^2\boldsymbol{u}^*, \quad \text{with} \quad \nabla\cdot\boldsymbol{u}^* = 0, \tag{5}$$

backwards from $t = \tau$ to $t = 0$ after initiating the adjoint velocity as $\boldsymbol{u}_\tau^*$ and implementing zero Dirichlet conditions on the control boundary [9].

2.3. Lagrangian functional

For a flow perturbed by both initial and boundary perturbations, the contribution of initial and boundary perturbations to the final velocity vector can be decomposed as a consequence of the linearisation:

$$\boldsymbol{u}_\tau = \boldsymbol{u}_{i\tau} + \boldsymbol{u}_{c\tau},$$

where $\boldsymbol{u}_{c\tau} = \mathcal{N}\boldsymbol{c}$ is the response of the flow field to the boundary perturbation while $\boldsymbol{u}_{i\tau}$ is the transient outcome of a given initial perturbation at $t = \tau$ and is considered to be a known velocity vector. The kinetic energy of the controlled flow field at $t = \tau$ is

$$E = (\boldsymbol{u}_\tau, \boldsymbol{u}_\tau) = (\boldsymbol{u}_{i\tau}, \boldsymbol{u}_{i\tau}) + [2\mathcal{N}^*\boldsymbol{u}_{i\tau} + \mathcal{N}^*\mathcal{N}\boldsymbol{c}, \boldsymbol{c}],$$

where the first term after the second equality is the energy of the uncontrolled outcome of the initial perturbation and the second term is a function of the control perturbation. Note that the dual relationship (3) is used to obtain this expression.

Taking into account the constraint on the control cost, we define a Lagrangian functional to minimise,

$$\mathcal{L} = E + \lambda(E_c - [\boldsymbol{c}, \boldsymbol{c}]), \tag{6}$$

where the first term is the total controlled energy and the second term is a constraint on the magnitude of the control. In the second term, λ is a Lagrangian multiplier and E_c can be interpreted as the control cost. This constraint on the magnitude of the control perturbation can be recovered by setting the first variation of the Lagrangian functional with respect to λ to zero.

Taking the first variation of the Lagrangian with respect to the control perturbation, we have

$$\delta\mathcal{L}(\delta\boldsymbol{c}) = [2\mathcal{N}^*\boldsymbol{u}_{i\tau} + 2\mathcal{N}^*\mathcal{N}\boldsymbol{c} - 2\lambda\boldsymbol{c}, \delta\boldsymbol{c}]. \tag{7}$$

Following the definition of a Gateau differential of a Lagrangian functional (see e.g. [15]), the gradient of the Lagrangian functional with respect to the control perturbation, denoted as $\nabla_{\boldsymbol{c}}\mathcal{L}$, can be evaluated as

$$\nabla_{\boldsymbol{c}}\mathcal{L} = 2\mathcal{N}^*\boldsymbol{u}_{i\tau} + 2\mathcal{N}^*\mathcal{N}\boldsymbol{c} - 2\lambda\boldsymbol{c}. \tag{8}$$

Clearly this gradient is a function of the uncontrolled transient response $\boldsymbol{u}_{i\tau}$, the control boundary perturbation $\boldsymbol{c}$ and an Lagrangian multiplier λ. The value of λ at the minimiser of the lagrangian functional can be obtained by setting this gradient to zero, so

$$\lambda = \frac{[\mathcal{N}^*\boldsymbol{u}_{i\tau} + \mathcal{N}^*\mathcal{N}\boldsymbol{c}, \boldsymbol{c}]}{[\boldsymbol{c}, \boldsymbol{c}]}. \tag{9}$$

We see that when the control cost E_c is small, $\boldsymbol{c}$ is small, and the magnitude of $\mathcal{N}\boldsymbol{c}$ is small compared with $\boldsymbol{u}_{i\tau}$. Therefore for sufficiently small control cost, the second and third terms on the right side of (8) are negligible compared with the first one. By removing these two terms, we see that the optimal control $\boldsymbol{c}$ is parallel with $\mathcal{N}^*\boldsymbol{u}_{i\tau}$ but with an opposite direction:

$$\boldsymbol{c} = -\mathcal{N}^*\boldsymbol{u}_{i\tau}\sqrt{E_c}/[\mathcal{N}^*\boldsymbol{u}_{i\tau}, \mathcal{N}^*\boldsymbol{u}_{i\tau}]^{1/2}.$$

In the following, this solution will be denoted as the sensitivity solution, since its distribution represents the sensitivity of the perturbations in the domain on boundary control, as similarly documented in base flow modification studies [12–14]. Such a solution can be used to choose the location of actuators in feed-back control. We note that the calculation of the sensitivity solution only requires a solo integration of the adjoint equations (the action of $\mathcal{N}^*$ on $\boldsymbol{u}_{i\tau}$).

2.4. Optimisation procedure

As presented above, the optimisation of the control forcing at a given control cost involves the computation of the minimiser of a Lagrangian functional, and the integration of the linearised NS equations and the adjoint equations. The optimisation procedures can be summarised as follows.

1. Initialise the adjoint Eq. (5) with $\boldsymbol{u}^*(\tau) = \boldsymbol{u}_{i\tau}$, which can be the outcome of the optimal initial perturbation, and integrate backwards to calculate $\mathcal{N}^*\boldsymbol{u}_{i\tau}$ through (4).
2. Initialise $\boldsymbol{c}$ using random noise and integrate the LNS Eq. (1) to obtain $\mathcal{N}\boldsymbol{c}$.
3. Integrate the adjoint Eq. (5) to obtain $\mathcal{N}^*\mathcal{N}\boldsymbol{c}$.
4. Substitute $\mathcal{N}^*\boldsymbol{u}_{i\tau}$ and $\mathcal{N}^*\mathcal{N}\boldsymbol{c}$ into (8) to calculate $\nabla_{\boldsymbol{c}}\mathcal{L}$.
5. Calculate the search direction $\mathcal{P}(\nabla_{\boldsymbol{c}}\mathcal{L})$ as presented in Appendix A and evolve the result using the LNS Eq. (1) to obtain $\mathcal{N}\mathcal{P}$.
6. Calculate the optimal step length α_{opt} following the procedure outlined in Appendix A, and update $\boldsymbol{c}$ and $\mathcal{N}\boldsymbol{c}$ from step k to $k+1$ along direction $\mathcal{P}$,
$$\tilde{\boldsymbol{c}}^{k+1} = \boldsymbol{c}^k + \alpha_{opt}\mathcal{P}, \qquad \text{and} \qquad \mathcal{N}\tilde{\boldsymbol{c}}^{k+1} = \mathcal{N}\boldsymbol{c}^k + \alpha_{opt}\mathcal{N}\mathcal{P}.$$
7. Scale the updated results in step 6 to satisfy the constraint on control cost:
$$\boldsymbol{c}^{k+1} = \beta\tilde{\boldsymbol{c}}^{k+1} \text{ and } \mathcal{N}\boldsymbol{c}^{k+1} = \beta\mathcal{N}\tilde{\boldsymbol{c}}^{k+1} \text{ with } \beta = \left(\frac{E_c}{[\tilde{\boldsymbol{c}}^{k+1}, \tilde{\boldsymbol{c}}^{k+1}]}\right)^{1/2}.$$
8. Repeat steps 3–7 until the solution $\boldsymbol{c}$ converges.

2.5. Uniqueness of the optimal boundary perturbation

In this section, we demonstrate that the Lagrangian functional defined in (6) has only one minimiser at each given value of control cost E_c even though this function is not convex, and therefore the optimal control obtained from the calculation procedure in Section 2.4 is unique.

At the equilibrium state where the gradient $\nabla_{\boldsymbol{c}}\mathcal{L}$ vanishes, we have

$$\mathcal{N}^*\boldsymbol{u}_{i\tau} + \mathcal{N}^*\mathcal{N}\boldsymbol{c} - \lambda\boldsymbol{c} = 0. \tag{10}$$

Here λ can be considered as a function of $\boldsymbol{c}$ defined in (9). Evaluating the second variation of the Lagrangian functional with respect to $\boldsymbol{c}$ at this equilibrium state, we obtain

$$\delta^2\mathcal{L}(\delta\boldsymbol{c}) = 2[\mathcal{N}^*\mathcal{N}\delta\boldsymbol{c}, \delta\boldsymbol{c}] - 2\lambda[\delta\boldsymbol{c}, \delta\boldsymbol{c}].$$

Here the joint operator $\mathcal{N}^*\mathcal{N}$ is self-adjoint, and therefore when this operator is discretised to form an $N \times N$ matrix, with N denoting the dimension of the discretised velocity variable, this matrix has N real and non-negative eigenvalues and N orthogonal eigenvectors. We denote the eigenvalue and eigenvector pair of this matrix as λ_i and $\boldsymbol{v}_i$ ($i = 1, \ldots, N$), where $0 \le \lambda_1 \le \lambda_2, \ldots, \lambda_N$ and $\boldsymbol{v}_i$ is normalised so that $[\boldsymbol{v}_i, \boldsymbol{v}_i] = 1$. Therefore the eigenvectors $\boldsymbol{v}_i$ form a complete base on $\mathbb{R}^N$ and the variation of $\boldsymbol{c}$ can be projected onto this basis as

$$\delta\boldsymbol{c} = \sum_{i=1}^{N} a_i\boldsymbol{v}_i.$$

Then we have

$$\delta^2\mathcal{L}(\delta\boldsymbol{c}) = \sum_{i=1}^{N} 2a_i^2(\lambda_i - \lambda).$$

If $\lambda \ge \lambda_N$, $\delta^2\mathcal{L} \le 0$, and this equilibrium state is a maximum; if $\lambda \le \lambda_1$, $\delta^2\mathcal{L} \ge 0$, and this equilibrium state is a minimum; if $\lambda_1 < \lambda < \lambda_N$, the sign of $\delta^2\mathcal{L}$ is undetermined, and this equilibrium state is an inflection point.

To illustrate that there is only one solution of $\boldsymbol{c}$ satisfying $\lambda(\boldsymbol{c}) \le \lambda_1$, we first decompose $\mathcal{N}^*\boldsymbol{u}_{i\tau}$ and $\boldsymbol{c}$ as a linear summation of the eigenvectors of $\mathcal{N}^*\mathcal{N}$,

$$\mathcal{N}^*\boldsymbol{u}_{i\tau} = \sum_{i=1}^{N} b_i\boldsymbol{v}_i \quad \text{and} \quad \boldsymbol{c} = \sum_{i=1}^{N} c_i\boldsymbol{v}_i,$$

and substitute them into (10) to reach

$$b_i + \lambda_i c_i = \lambda c_i \quad \text{with} \quad 1 \le i \le N. \tag{11}$$

Considering the constraint on control cost, i.e. $E_c - [\boldsymbol{c}, \boldsymbol{c}] = 0$, we have $\sum_{i=1}^{N} c_i^2 = E_c$. Then we define a function

$$F(\sigma) = \sum_{i=1}^{N} \frac{b_i^2}{(\sigma - \lambda_i)^2} - E_c. \tag{12}$$

Combining (11) and (12), we see that λ is the root of function $F(\sigma)$. This function is monotonic for $\sigma \in (-\infty, \lambda_1]$ with $F(-\infty) = -E_c < 0$ and $F(\lambda_1) = \infty > 0$. Therefore the function $F(\sigma)$ has only one root in

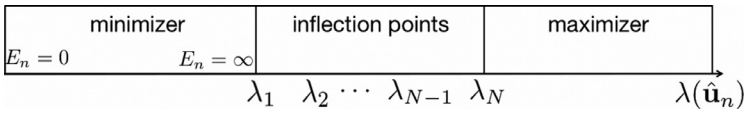

Fig. 1. Illustration of λ as a function of the minimum, maximum and inflection points of the Lagrangian functional.

the range $\in (-\infty, \lambda_1]$ and this root is λ. Therefore for a given control cost E_c, λ is unique. From (11), we see that this unique value of λ corresponds to a unique sequence of c_i and so a unique solution of $\boldsymbol{c}$.

It is observed in (12) that as E_c increases, λ is closer to λ_1 and the weight of $\boldsymbol{v}_1$ in the optimal perturbation, $c_1 = b_1/(\lambda - \lambda_1)$, increases in magnitude faster than other c_i. When $E_c \to \infty$, $\lambda \to \lambda_1$ and $\boldsymbol{c} \to c_1\boldsymbol{v}_1$. Since $\boldsymbol{v}_1$ is discretisation-dependent and its spatial distribution is highly oscillatory, it can be expected that the optimal perturbation converges more slowly at higher values of control cost E_c.

It is noted that for $\lambda \in (-\infty, \lambda_1]$ there is singularity in (12) if $b_1 = 0$. At this singular condition, define a reduced version of functional $F(\sigma)$ as

$$F_r(\sigma) = \sum_{i=2}^{N} \frac{b_i^2}{(\sigma - \lambda_i)^2} - E_c.$$

This reduced function F_r is also monotonic for $\sigma \in (-\infty, \lambda_1]$. Then two possible solutions of $\lambda \in (-\infty, \lambda_1]$ and its associated $\boldsymbol{c}$ can be derived:

$$(i) \quad \lambda = \lambda_1 \text{ with } c_i = \frac{b_i}{\lambda_1 - \lambda_i} \text{ for } 2 \le i \le N \text{ and } c_1^2 = -F_r(\lambda_1).$$

$$(ii) \quad \lambda < \lambda_1 \text{ with } c_i = \frac{b_i}{\lambda - \lambda_i} \text{ for } 2 \le i \le N \text{ and } c_1 = 0.$$

If $F_r(\lambda_1) \le 0$, solution (i) is a valid solution while solution (ii) is not, because for solution (ii), $F(\lambda) = F_r(\lambda) < F_r(\lambda_1) \le 0$ and the constraint on control cost is broken. If $F_r(\lambda_1) > 0$, solution (i) is not valid since $c_i^2 < 0$ while solution (ii) is valid, since there exists $\lambda < \lambda_1$ satisfying $-E_c = F(-\infty) < F(\lambda) = 0 < F(\lambda_1) = F_r(\lambda_1)$. Therefore even when the singularity associated with $b_1 = 0$ exists, there is still only one minimum point for the Lagrangian functional in the range $\lambda \in (\infty, \lambda_1]$.

In summary, there is only one solution of λ in the range $(\infty, \lambda_1]$, and correspondingly the Lagrangian functional has only one minimiser for any given control cost while analogously it can be demonstrated that this Lagrangian functional has only one maximiser and potentially some inflection points, as illustrated schematically in Fig. 1.

2.6. Controllability analysis

As discussed above, an optimal boundary perturbation minimising the transient energy growth exists at a given control cost. In this section, we relax the constraint on control cost and calculate the optimal control across all values of the control cost. This "global" optimal control evaluates the controllability of the perturbations in the domain by boundary forcing. If partitioning the transient response to an initial perturbation into two parts: one that can be suppressed by boundary perturbations and the other that is out of the reach of boundary control and cannot be controlled regardless of the distribution and magnitude of the control, then the maximum control effect, which completely suppresses the first part, can be achieved by this "global" optimal control.

As discussed in Section 2.5, assume that the operator $\mathcal{N}^*\mathcal{N}$ is discretised into a $N \times N$ matrix. The eigenvalues and eigenvectors of this matrix are denoted as λ_i and $\boldsymbol{v}_i$, where $1 \le i \le N$. Then the eigenvectors $\boldsymbol{v}_i$ can be projected from the control boundary $\partial\Omega$ to the computational domain Ω by integrating LNS equations to reach orthogonal vectors $\mathcal{N}\boldsymbol{v}_i$,

$$(\mathcal{N}\boldsymbol{v}_i, \mathcal{N}\boldsymbol{v}_j) = [\mathcal{N}^*\mathcal{N}\boldsymbol{v}_i, \boldsymbol{v}_j] = \lambda_i[\boldsymbol{v}_i, \boldsymbol{v}_j] = \begin{cases} \lambda_i, & i = j \\ 0, & i \ne j \end{cases}$$

Since the dimension of the boundary perturbations is smaller than that of its response field, this orthogonal space $(\mathcal{N}\boldsymbol{v}_1, \mathcal{N}\boldsymbol{v}_2, \ldots, \mathcal{N}\boldsymbol{v}_N)$ defined in Ω does not form a complete basis. Therefore the transient response field to be controlled can be decomposed as

$$\boldsymbol{u}_{i\tau} = \sum_{i=1}^{N} d_i \mathcal{N}\boldsymbol{v}_i + \boldsymbol{u}_{out}$$

where $\boldsymbol{u}_{out}$ denotes the component of $\boldsymbol{u}_{i\tau}$ that cannot be projected to this incomplete space and thus is uncontrollable by boundary perturbations.

The energy of $\boldsymbol{u}_{out}$ quantitatively describes the controllability of $\boldsymbol{u}_{i\tau}$ using boundary perturbation control. The energy associated with this uncontrollable component is

$$\begin{aligned} E_g = (\boldsymbol{u}_{out}, \boldsymbol{u}_{out}) &= \min_{\boldsymbol{c}} \left(\boldsymbol{u}_{i\tau} - \frac{(\boldsymbol{u}_{i\tau}, \mathcal{N}\boldsymbol{c})}{(\mathcal{N}\boldsymbol{c}, \mathcal{N}\boldsymbol{c})}\mathcal{N}\boldsymbol{c}, \boldsymbol{u}_{i\tau} - \frac{(\boldsymbol{u}_{i\tau}, \mathcal{N}\boldsymbol{c})}{(\mathcal{N}\boldsymbol{c}, \mathcal{N}\boldsymbol{c})}\mathcal{N}\boldsymbol{c} \right) \\ &= \min_{\boldsymbol{c}} \left((\boldsymbol{u}_{i\tau}, \boldsymbol{u}_{i\tau}) - \frac{[\mathcal{N}^*\boldsymbol{u}_{i\tau}, \boldsymbol{c}]^2}{[\mathcal{N}^*\mathcal{N}\boldsymbol{c}, \boldsymbol{c}]} \right). \end{aligned}$$

Here the subscript g indicates that the controlled total energy, reached at the "global" optimal control — over all the values of control cost or without constraint on the magnitude of the control perturbation.

Since there is no constraint on the control cost, the total energy E_g can be considered as the objective functional to minimise. The gradient of E_g with respect to $\boldsymbol{c}$ is

$$\nabla_{\boldsymbol{c}} E_g = 2\frac{[\mathcal{N}^*\boldsymbol{u}_{i\tau}, \boldsymbol{c}]^2}{[\mathcal{N}^*\mathcal{N}\boldsymbol{c}, \boldsymbol{c}]^2}\mathcal{N}^*\mathcal{N}\boldsymbol{c} - 2\frac{[\mathcal{N}^*\boldsymbol{u}_{i\tau}, \boldsymbol{c}]}{[\mathcal{N}^*\mathcal{N}\boldsymbol{c}, \boldsymbol{c}]}\mathcal{N}^*\boldsymbol{u}_{i\tau}. \tag{13}$$

Similarly as presented in Section 2.4, the global optimal control $\boldsymbol{c}_g$ can be obtained. The magnitude of this control can be evaluated by the control cost $E_{cg} = [\boldsymbol{c}_g, \boldsymbol{c}_g]$.

Setting $\nabla_{\boldsymbol{c}} E_g$ to zero, we notice that the distribution of this "global" optimal perturbation can be analytically expressed as $(\mathcal{N}^*\mathcal{N})^{-1}\mathcal{N}^*\boldsymbol{u}_{i\tau}$. $\mathcal{N}^*\mathcal{N}$ is a self-adjoint operator with real eigenvalues, and when acting on a perturbation vector, its largest eigenvalue (and the corresponding most energetic eigenmode) presents the dominant amplification effect. However, when its inverse, i.e. $(\mathcal{N}^*\mathcal{N})^{-1}$, acting on a perturbation, the smallest eigenvalue (and the corresponding least energetic eigenmode) of $\mathcal{N}^*\mathcal{N}$ becomes dominant. We note that as a continuous operator, $\mathcal{N}^*\mathcal{N}$ does not have a least energetic eignenmode. However when $\mathcal{N}^*\mathcal{N}$ is discretised, this eigenmode can be calculated, even though it is discretisation-dependent and becomes more spatially oscillatory as the discretisation is refined. Therefore we expect that the "global" optimal perturbation will converge slowly and is spatially highly oscillatory.

It is worth noting that the optimal perturbation $\boldsymbol{c}_g$ is also the equilibrium state of $\mathcal{L}$ at control cost $E_c = E_{cg}$ and corresponds to $\lambda = 0$. As the resolution increases, $\lambda_1 \to 0$, and $\boldsymbol{c}_g$ tends to be parallel with $\boldsymbol{v}_1$, inducing poor convergence. This analysis also suggests that the control cost E_c should not exceed E_{cg}, since any extra cost does not contribute to suppressing the transient effects.

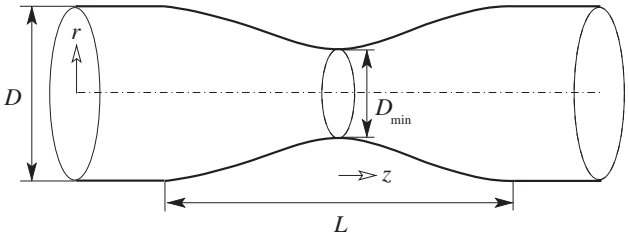

Fig. 2. Stenosis geometry, with a co-sinusoidal shape, $L = 2D$ and $D = 2D_{min}$.

3. Case 1—steady stenotic flow

In this section, we test the methodology introduced above in the context of an open, wall-bounded flow: stenotic flow. The geometry of the stenotic flow is introduced in Section 3.1, a convergence test is conducted in Section 3.2 and then the optimal wall-normal boundary perturbation is calculated to optimally suppress the transient energy growth induced by the global optimal initial perturbation and the controllability analysis is also conducted by relaxing constraint on the control cost in Section 3.3. The optimal initial perturbation and its outcome are adopted as the control objective because they are also the focal of feed-back control of noise developments. It will be shown that while the boundary transpiration is applied without restriction all along the outer wall of the domain, in practice the optimal boundary perturbation is highly localised near the stenotic contraction.

3.1. Problem description

As shown in Fig. 2, the stenosis has a 75% co-sinusoidal occlusion and a length which is twice the upstream pipe diameter, D. We adopt a cylindrical coordinate system with its origin at the centre of the stenosis throat. The (axial, radial, azimuthal) position coordinates are (z, r, θ). Velocities are normalised by the bulk flow speed $\overline{u}$ of the upstream Hagen–Poiseuille flow, and the length scale adopted is the upstream pipe diameter D, giving $D/\overline{u}$ as the time scale, and Reynolds number $Re = \overline{u}D/\nu$, as used in a previous work [20]. Hereafter in this case study we adopt dimensionless variables based on these normalisations. We consider the Reynolds number $Re = 400$ for which the base flow is asymptotically stable; the same Reynolds number was the main focus of attention in the transient growth study in [21]. At $Re = 400$, the maximum energy growth of initial perturbations, 8.94×10^4, occurs for a dimensionless time horizon $\tau = 4.43$ at azimuthal wavenumber $m = 1$ [21]. In the remainder of this section, $m = 1$ is adopted and the outcome of the related global optimal initial perturbation at $t = 4.43$ is considered as the control target $\boldsymbol{u}_{i\tau}$. The optimal initial perturbation is normalised such that the initial state energy is $(\boldsymbol{u}_{t=0}, \boldsymbol{u}_{t=0}) = 1$ and therefore the uncontrolled final state energy is $(\boldsymbol{u}_{i\tau}, \boldsymbol{u}_{i\tau}) = 8.94 \times 10^4$.

3.2. Discretisation and convergence test

Spectral elements employing piecewise continuous nodal-based polynomial expansions within mapped-quadrilateral elemental subdomains are adopted for spatial discretisation of the axisymmetric geometry in the meridional semi-plane, coupled with a Fourier decomposition in azimuth. Since the azimuthal velocity for the base flow is zero, a complex mode for perturbations with azimuthal wavenumber m can be further decomposed to a pair of modes [22].

Time integration is carried out using a second-order-time velocity-correction scheme. Details of the discretisation and its convergence properties are given in [23]. The same numerics are used to compute base flows and the actions of the LNS and adjoint operators. The temporal dependence function $f(t, \omega)$, which eliminates the spatial discontinuities at $t = 0$ and $t = \tau$ is defined as

$$f(t, \omega) = (1 - e^{-t^2})(1 - e^{-(t-\tau)^2}) \cos(\omega t). \quad (14)$$

Therefore the adjoint operator $f^*(t, \omega) = f(t, \omega)$. This function is purely real since we have decomposed the complex mode to a pair of modes with restricted symmetry. This time-dependence function with $\tau = 10$ and $\omega = 5$ is illustrated in Fig. 3, where we see that it effectively sets the boundary perturbation $\boldsymbol{u}_c$ to zero at the beginning and end of the computation. Therefore the boundary conditions and initial conditions are compatible for both the LNS equations and the adjoint equations [9].

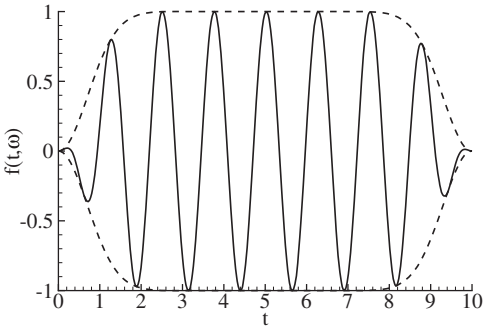

Fig. 3. The temporal dependence of the boundary velocity perturbation in the stenotic flow, $f(t, \omega)$, as defined in (14). The dashed line represents the envelope of this function.

Table 1
Convergence of λ_N with respect to both mesh and the tensor product polynomial order P for the stenotic flow at $Re = 400$, $\omega = 0$ and $\tau = 4.43$.

Mesh	P	λ_N
A	3	7.97994×10^4
A	4	8.00318×10^4
A	5	8.00358×10^4
A	6	8.00361×10^4
A	7	8.00361×10^4
A	8	8.00361×10^4
B	6	8.00361×10^4
C	6	8.00361×10^4

As a convergence test we calculate λ_N, i.e. the largest eigenvalue of $\mathcal{N}^*\mathcal{N}$. Three structured grids, denoted as "A", "B", "C" , are tested. Mesh "A" consisting of an array of (streamwise $\times$ vortical) 187×9 elements is illustrated in Fig. 4. Meshes "B" and "C" are denser in z and y directions compared with "A", consisting of arrays of 219×9 and 187×11 elements, respectively.

On the inflow and outflow boundaries, zero-Dirichlet and computed Neumann conditions are used for velocity and pressure respectively in both forward and backward integrations. On the solid wall, optimal control and zero Dirichlet conditions are used for the velocity components in the forward and backward integrations respectively while the pressure condition is a computed Neumann type for both integrations [24]. On the axis, boundary conditions depend on the azimuthal wave number m and solution variable, and these are zero-Dirichlet or zero-Neumann [23]. The initial condition for the forward system is set to zero while the backward integration is initialised by the outcome of the forward integration [9].

Convergence of λ_N with respect to the tensor-product polynomial order P in the spectral element mesh is presented in Table 1. We see that the result has converged to five significant figures at $P = 5$ for mesh "A" and is insensitive to further mesh refinement. In the following calculations, mesh "A" is adopted with $P = 5$.

The variation of λ_N with ω is presented in Fig. 5(a) for $\tau = 4.43$, where we see λ_N reaches a maximum at $\omega = 7.5$. The corresponding profiles of eigenvectors, which are optimal wall-normal

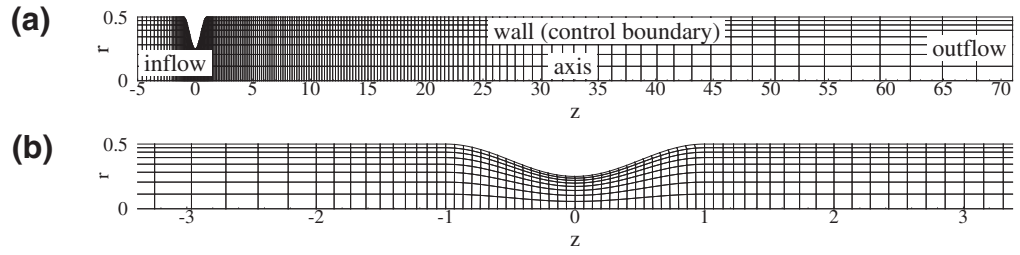

Fig. 4. Spectral element mesh for the stenotic flow: (a) overall mesh (note use of expanded radial scale), and (b) mesh around the contraction section (true aspect ratio).

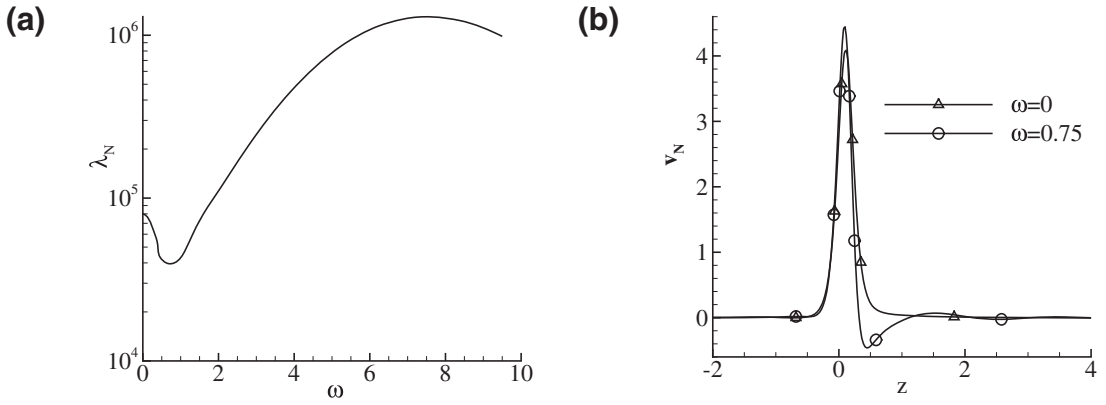

Fig. 5. (a) Variation of the largest eigenvalue λ_N, i.e. the gain of the optimal boundary perturbation, with temporal frequency ω at $\tau = 4.43$ and (b) profiles of $\boldsymbol{v}_N$, i.e. the optimal boundary perturbation, at $\omega = 0$ and $\omega = 7.5$ for the stenotic flow. The perturbation for $z \in [-5, -2] \bigcup [4, 70]$ is negligible and not represented.

boundary perturbations that generate maximum energy growth over τ, are shown in Fig. 5(b). Since the optimal wall-normal boundary perturbation is concentrated in the contraction section, we have truncated the range of z represented from $[-5, 70]$ to $[-2, 4]$ in order to better illustrate the distribution of the perturbation.

3.3. Results

To demonstrate the proposed optimisation method, we calculate the boundary perturbation that minimises the transient effect of the global optimal initial perturbation obtained at $Re = 400$, corresponding to $m = 1$ and $\tau = 4.43$ with energy growth $G = 8.94 \times 10^4$ [21].

The effectiveness of using boundary perturbations to control the transient effect can be modelled as

$$J = \frac{(\boldsymbol{u}_{i\tau}, \boldsymbol{u}_{i\tau}) - E}{E_c}, \tag{15}$$

where the numerator is the transient energy suppressed by the control and the denominator is the control cost (see Fig. 6).

Comparing with Fig. 5(a), we notice that the control effectiveness is not as sensitive to the frequency as the gain of boundary perturbations. It is also observed that the effectiveness drops for increasing control cost. At the smallest value of E_c considered, the control effectiveness reaches 10^8. This is because when the control is small enough, the effectiveness can be approximated as $2(\mathcal{N}\boldsymbol{c}, \boldsymbol{u}_{i\tau})/E_c$, where $\mathcal{N}\boldsymbol{c}$ and $\boldsymbol{u}_{i\tau}$ take advantage of the amplification of the base flow to boundary and initial perturbations respectively, resulting in a large value of control effectiveness. The solution converges slowly for $E_c > 10^4$ and at this range of E_c, the effectiveness has dropped significantly compared with that at low levels of E_c. Therefore higher values of E_c have not been examined.

The control cost at which the energy E is minimised at a fixed frequency ω can be obtained from the controllability analysis, as shown in Fig. 7(a). It is noted that the control cost to cancel as much transient energy as possible varies with the frequency dramatically and the minimum control cost is obtained around $\omega = 5$. The transient

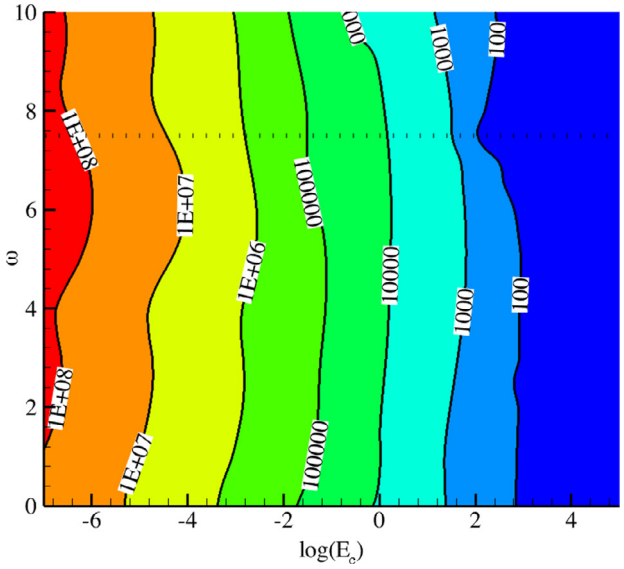

Fig. 6. Contour of control effectiveness J, as defined in (15) at various control costs and frequencies for the stenotic flow.

effect that cannot be controlled by boundary perturbations, represented as E_g, are not sensitive to the frequency and therefore we define a variable to denote the global effectiveness of control as

$$J_g = \frac{(\boldsymbol{u}_{i\tau}, \boldsymbol{u}_{i\tau}) - E_g}{E_{cg}}, \tag{16}$$

which evaluates the ratio of suppressed transient energy and the control cost (see Fig. 7(b)).

In the following we focus on two cases: one with $\omega = 5$, which is indicated from the controllability analysis as the "global" optimal frequency and the other with $\omega = 0$, which corresponds a steady

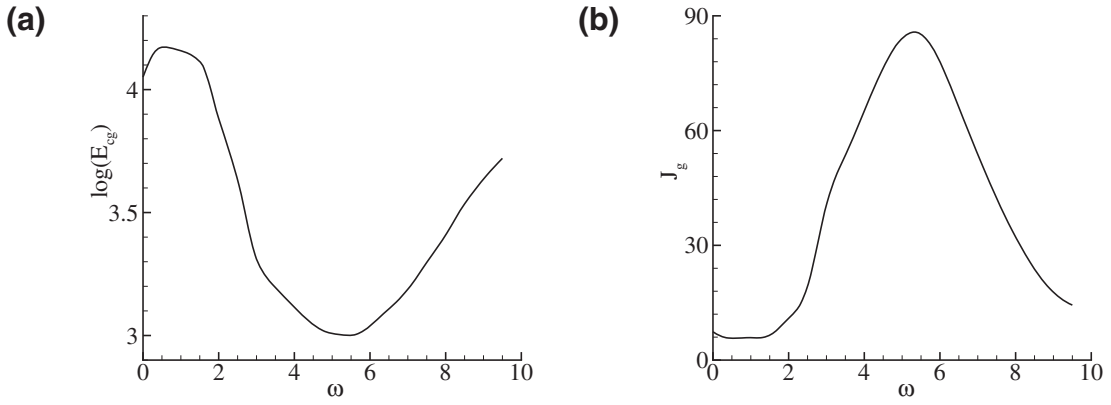

Fig. 7. (a) The control cost at various frequencies obtained from controllability analyses and (b) global control effectiveness from controllability analyses, defined in (16), for the stenotic flow.

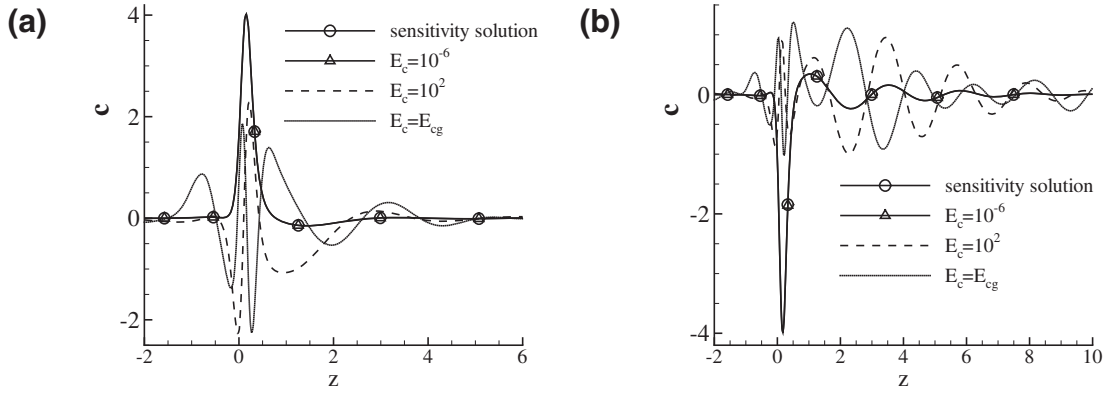

Fig. 8. Distribution of the optimal boundary perturbations to the stenotic flow at (a) $\omega = 0$ and (b) $\omega = 5$.

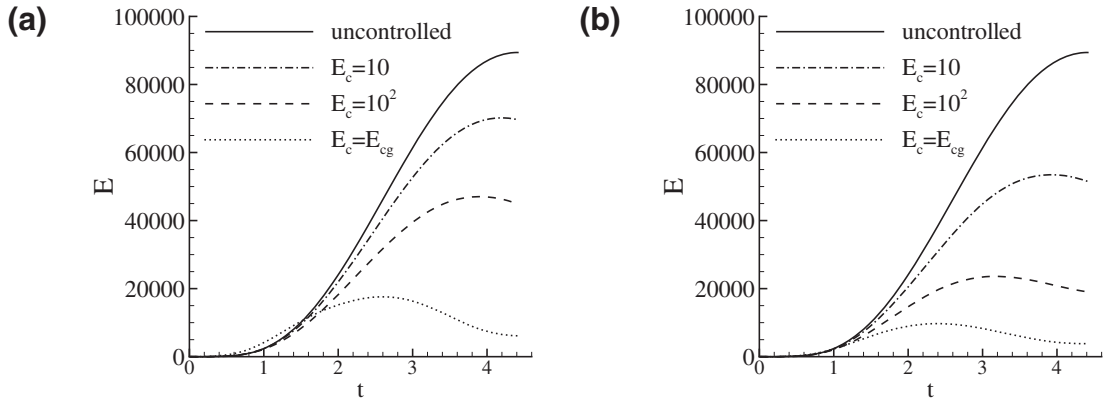

Fig. 9. Energy history of the controlled and uncontrolled evolution of the global optimal initial perturbation to the stenotic flow at (a) $\omega = 0$ and (b) $\omega = 5$.

boundary control except at the beginning and end of the time horizon considered.

The optimal perturbations at $\omega = 0$ are plotted in Fig. 8(a). To compare the distribution of optimal perturbations at various control costs, the perturbations are normalised so that $[\boldsymbol{c}, \boldsymbol{c}] = 1$. We see that at small values of control cost E_c, the optimal perturbation almost overlaps with the sensitivity solution, which is parallel and opposite with $\mathcal{N}^*\boldsymbol{u}_{i\tau}$, as expected. At higher values of E_c, the weight of $\boldsymbol{v}_1$, i.e. the least energetic mode whose distribution is grid dependent, increases in the optimal boundary perturbation, and therefore results in a more oscillatory profile. $\boldsymbol{c}_g$ is the optimal perturbation calculated from controllability analyses corresponding to control cost $E_{cg} = 1.52 \times 10^4$. This global optimal solution across all values of control costs is also highly oscillatory and the energy distribution spreads from the contraction segment to the downstream segment. The same results for $\omega = 5$ is shown in Fig. 8(b), where the global optimal solution $\boldsymbol{c}_g$ corresponds to $E_{cg} = 1.36 \times 10^3$.

The evolution of energy for both controlled and uncontrolled conditions is illustrated in Fig. 9, where we see that the transient effect is suppressed significantly by the boundary perturbations and under the control of $\boldsymbol{c}_g$, over 95% of the transient energy growth is cancelled.

We note that the controlled energy can be decomposed as $(\boldsymbol{u}_{it}, \boldsymbol{u}_{it}) + 2(\boldsymbol{u}_{it}, \boldsymbol{u}_{ct}) + (\boldsymbol{u}_{ct}, \boldsymbol{u}_{ct})$, where $\boldsymbol{u}_{it}$ and $\boldsymbol{u}_{ct}$ are the perturbations at time t induced by the initial perturbation and boundary control, respectively. The first term is the uncontrolled energy, the second one denotes the interaction of the control and the objective

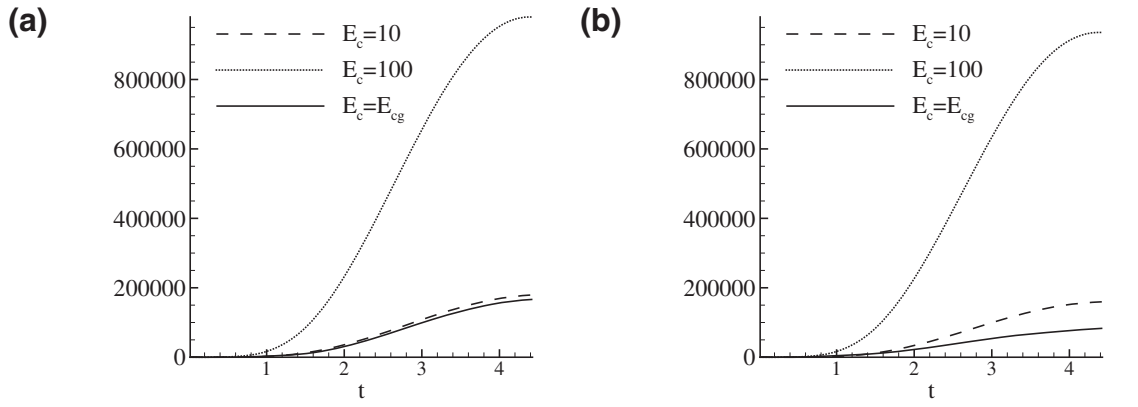

Fig. 10. (a) $-2(\boldsymbol{u}_{it}, \boldsymbol{u}_{ct})$ and (b) $(\boldsymbol{u}_{ct}, \boldsymbol{u}_{ct})$ at $\omega = 0$ for the stenotic flow.

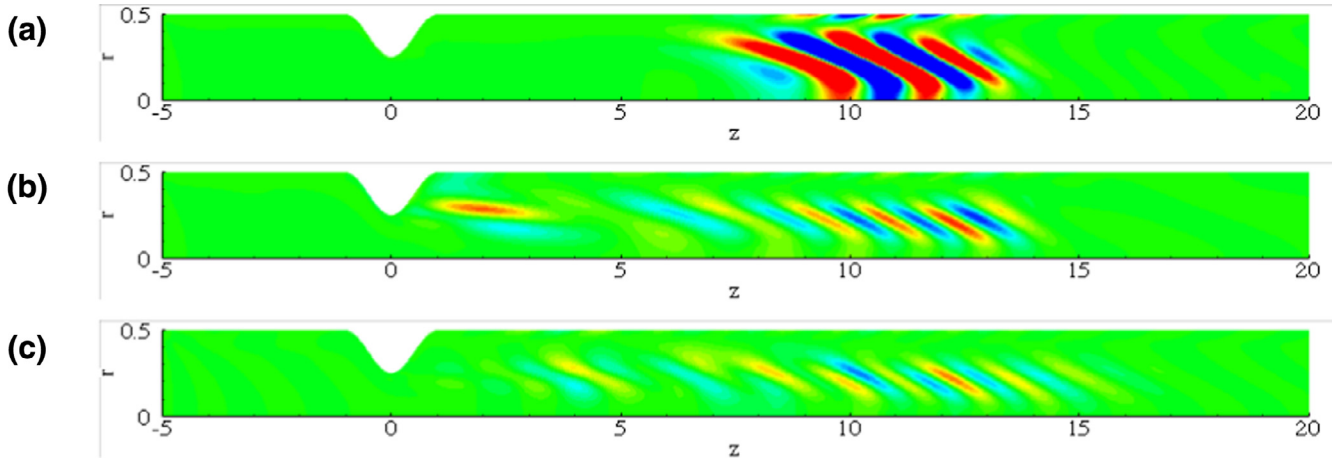

Fig. 11. Contours of azimuthal vorticity for outcome of the optimal initial perturbation to the stenotic flow at $t = \tau = 4.43$. (a) without control; (b, c) with control $\boldsymbol{c}_g$ at $\omega = 0$ and $\omega = 5$ respectively. .

perturbation, and the last one is induced by the control. Considering that the control reduces the total energy, the second term is negative, while the last one is positive. The control effect depends on the balance of the last two terms, as illustrated in Fig. 10. We see that when E_c increases from 10 to 100, both terms (the interaction term is reversed to be positive) rise to values significantly larger than the uncontrolled energy, and therefore the control effect is realised by the difference of two large terms. At E_{cg}, the interaction term is much larger than the control induced term, indicating that the control effect becomes more efficient than the $E_c = 10$ and 100 cases.

The final outcomes of the controlled and uncontrolled flow field are presented in Fig. 11. Clearly under the optimal control $\boldsymbol{c}_g$ obtained at $\omega = 0$ and $\omega = 5$, the final perturbation has spread to a larger space owing to the continuous control perturbation, which keeps the close downstream region of the contraction section perturbed. Nevertheless, the total energy is dramatically lower than that of the uncontrolled perturbation.

4. Case 2—Batchelor vortex flow

In this section, we implement the optimal control methodology in the context of an open unbounded flow, the Batchelor vortex flow. The mathematical model and stability characteristics of the Batchelor flow are introduced in Section 4.1; a convergence test is conducted in Section 4.2; and then the optimal inflow-normal boundary perturbation is calculated to suppress the transient energy growth induced by the global optimal initial perturbation, and direct numerical simulations (DNS) are conducted to study the control effects on spiral vortex breakdown in Section 4.3.

4.1. Problem description

The Batchelor vortex can be represented in cylindrical coordinates (z, r, θ) as [25]

$$\bar{u}(r) = a + \mathrm{e}^{-r^2}, \qquad \bar{v}(r) = 0, \qquad \bar{w}(r) = q/r(1 - \mathrm{e}^{-r^2}),$$

where a denotes the external non-dimensional free-stream axial velocity. The streamwise velocity maximises at $r = 0$ and reduces monotonically in the radial direction, while the azimuthal velocity maximises at $r = 1.12$, which can be considered as a measurement of the vortex core. It has been noted by [26] that the translation and inversion of the axial velocity $\bar{u}(r)$ do not affect the instability of the Batchelor vortex: they only affect the frequency but the growth rates remain unchanged. Therefore to simplify the model, $a = 0$ is adopted throughout this study. The parameter q is the swirl strength and for $q < 2.31$ the Batchelor vortex is unstable in the inviscid limit [27,28]. In this work we adopt $q = 0.8$ in order to energise the helical instabilities which initiate the spiral vortex breakdown [29,30]. In this case, the Reynolds number is defined as $Re = \Delta\bar{u}\mathrm{R}_0/\nu$, where $\Delta\bar{u}$ is the dimensional velocity excess in the core of the vortex, R_0 is a measurement of the radius of the vortex core and ν is the kinematic viscosity. In this case study, the Reynolds number is set to $Re = 1000$ in the interest of balancing values of practical interest against computational cost.

4.2. Discretisation and convergence test

The numerical method is the same as used in Section 3. Because the azimuthal velocity in the base flow is non-zero, the

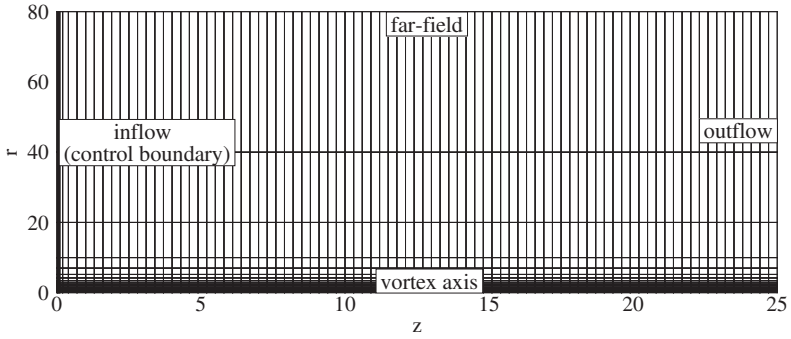

Fig. 12. Spectral subdomains for the Batchelor vortex.

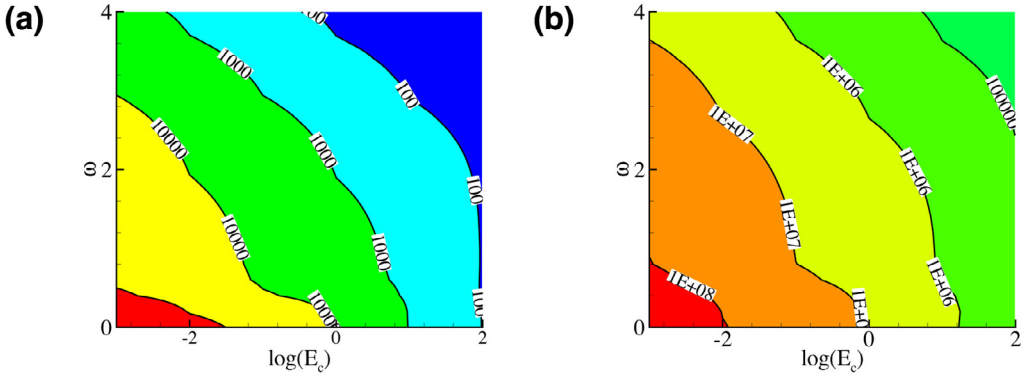

Fig. 13. Contour of control effectiveness J, defined in (15), at various control costs and frequencies for the vortex flow at azimuthal wavenumbers (a) $m = 1$ and (b) $m = 2$. The Reynolds number $Re = 1000$, swirl strength $q = 0.8$ and final time $\tau = 30$ are used here and in all the following plots.

perturbation is complex. Therefore we adopt a complex temporal dependence function $f(t, \omega)$,

$$f(t, \omega) = (1 - e^{-t^2})(1 - e^{-(t-\tau)^2})e^{i\omega t}. \tag{17}$$

We see that the adjoint operator $f^*(t, \omega) = f(t, -\omega)$. Clearly the real part of this function is the same as that used in the stenotic flow. This time-dependence function sets the boundary perturbation $\boldsymbol{u}_c(\boldsymbol{x}, t)$ to zero at the beginning and end of the computation to eliminate spatial discontinuity at the beginning of the forward and backward integrations [9].

The computational domain and boundaries are illustrated in Fig. 12. On the inflow boundary, Dirichlet-type control and zero Dirichlet conditions are used for the velocity components in the forward and backward integrations respectively while the computed Neumann conditions are used for pressure boundary conditions in both integrations. On the far-field boundary, zero-Dirichlet and computed Neumann conditions are used for velocity and pressure respectively in both forward and backward integrations. On the axis, boundary conditions depend on the azimuthal wave number as discussed in [23]. The outflow boundary deserves some special concerns. Since the developing of helical structures around the outflow boundary intuitively excludes the choice of zero-Dirichlet velocity condition for the forward integration, we adopt the combination of conditions for the forward and adjoint systems as presented in [11]. The initial condition for the forward system is set to zero while the backward integration is initialised by the outcome of the forward integration [9].

As a convergence test we calculate the optimal initial perturbations and optimal inflow boundary perturbations which induce largest energy growth over a fixed time interval $\tau = 30$, which will be used as the defaulted value of final time in this section. The convergence of G (the largest energy growth induced by the optimal initial perturbation) and λ_N with respect to the polynomial order P used in the polynomial expansion in each spectral element is presented in Table 2. We see that at $P = 5$, both G and λ_N have converged to within tolerance 0.01. In all the following calculations in this case, we adopt $P = 5$, the same as used in the case of stenotic flow.

Table 2
Convergence of G and λ_N with respect to the polynomial order P at $Re = 1000$, $\omega = 0$, $m = 3$ and $\tau = 30$.

P	G	λ_N
3	1.5956×10^8	3.0376×10^4
4	1.5748×10^8	3.9649×10^4
5	1.5561×10^8	4.0465×10^4
6	1.5527×10^8	4.0683×10^4
7	1.5509×10^8	4.0734×10^4
8	1.5498×10^8	4.0745×10^4

4.3. Results

The optimal inflow perturbations are calculated to minimise the transient energy growth of the optimal initial perturbations associated with the helical instabilities of the Batchelor vortex. Two azimuthal wavenumbers, $m = 1$ and $m = 2$, are considered. The transient energy growth induced by the optimal initial perturbation is $G = 9.02 \times 10^3$ for $m = 1$ and $G = 1.53 \times 10^7$ for $m = 2$ for the computational domain and parameters considered ($\tau = 30$, $q = 0.8$ and $Re = 1000$). We note that the transient growth at $m = 2$ is much higher than that at $m = 1$. This is consistent with previous local stability studies, which revealed that the Batchelor vortex is much more unstable at $m = 2$ than at $m = 1$ (the maximum growth rate rises from around 0.17 at $m = 1$ to 0.31 at $m = 2$ in the inviscid limit) [26]. The initial perturbation is normalised to have unit energy and therefore the uncontrolled final state energy is $E = 9.02 \times 10^3$ and $E = 1.53 \times 10^7$ for $m = 1$ and $m = 2$, respectively.

The effectiveness of using boundary perturbations to control the transient effects is illustrated in Fig. 13. The solution converges slow for $E_c > 10^2$ and at this range of E_c, the effectiveness has dropped significantly compared with that at low levels of E_c. Therefore higher

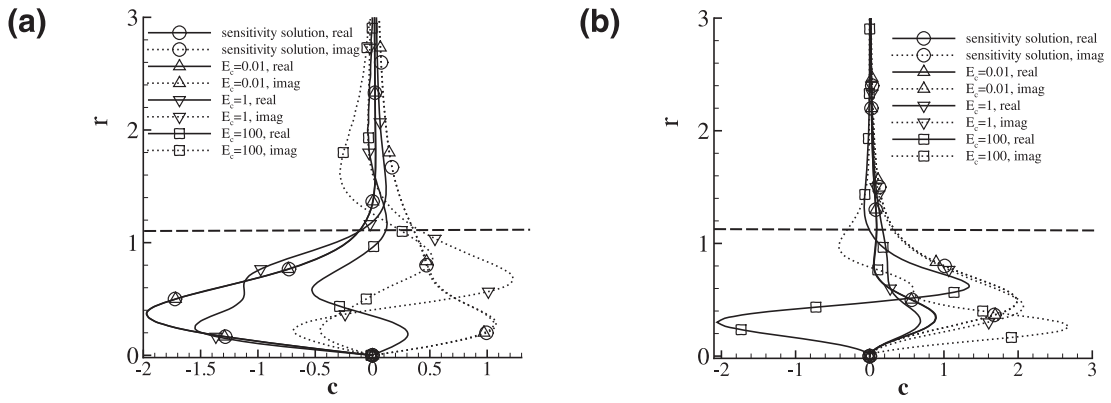

Fig. 14. Distribution of the optimal inflow control to the vortex flow at (a) $m = 1$ and (b) $m = 2$ with $\omega = 0$. "real" and "imag" denote the real and imaginary parts of the inflow-normal perturbation, respectively. The thick dashed lines represent the vortex radius $r = 1.12$.

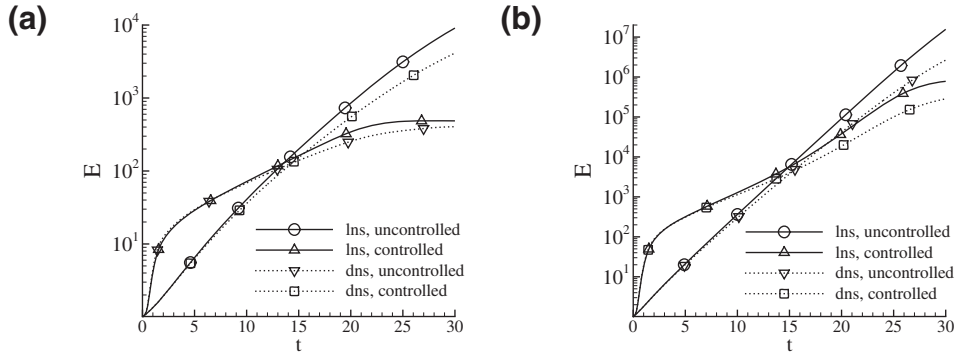

Fig. 15. Energy history of the controlled and uncontrolled evolution of the global optimal initial perturbation to the vortex flow at (a) $m = 1$, $E_c = 10$ and relative initial perturbation energy $l = 10^{-6}$ and (b) $m = 2$, $E_c = 100$ and $l = 10^{-8}$. "lns" represents the results of linearised evolution and "dns" denotes the nonlinear evolution obtained from DNS.

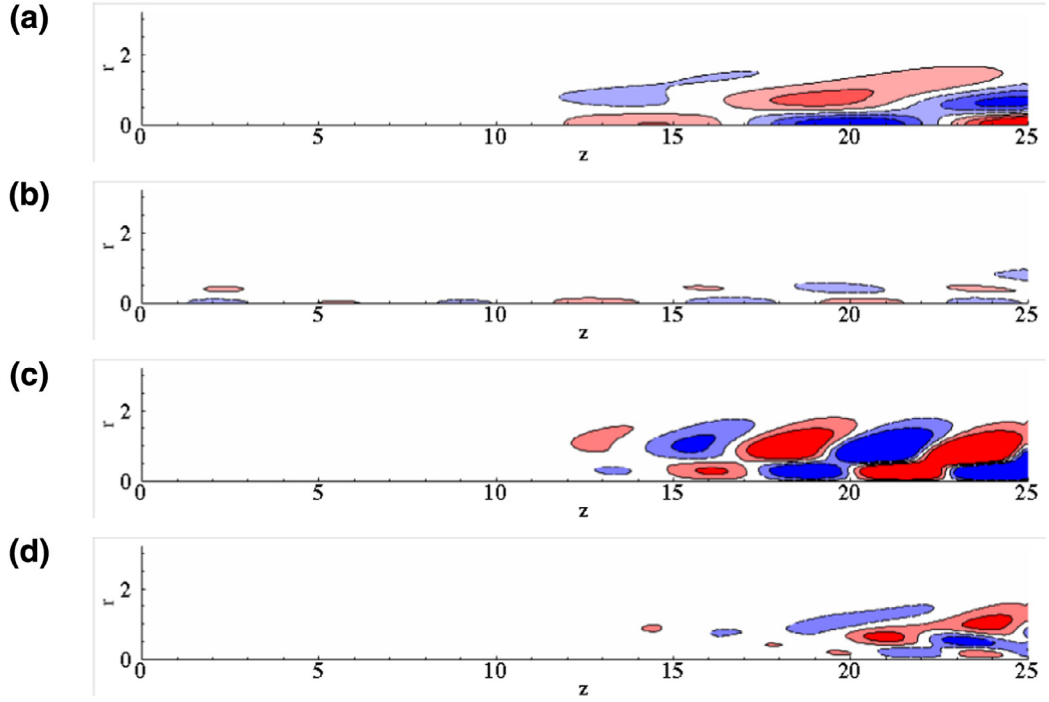

Fig. 16. Contours of azimuthal vorticity in linearised evolution of perturbations to the vortex flow at $t = \tau = 30$. (a, b) Uncontrolled and controlled evolution at $m = 1$; (c, d) uncontrolled and controlled evolution at $m = 2$. To verify the control effects, the same contour levels are used in the controlled and uncontrolled cases.

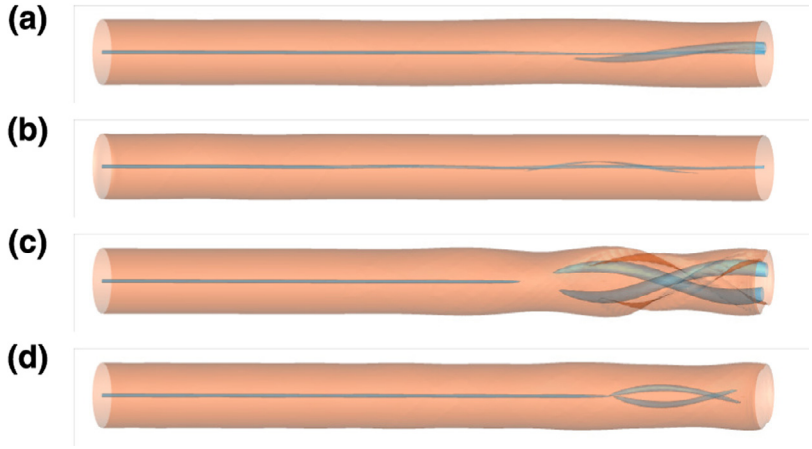

Fig. 17. Iso-surfaces of "λ_2" −0.5 and −0.001 in DNS of the Batchelor vortex flow initially perturbed by the optimal initial perturbation. (a, b) uncontrolled and controlled evolution at $m = 1$, $E_c = 10$ and $l = 10^{-6}$; (c, d) uncontrolled and controlled evolution at $m = 2$, $E_c = 100$ and $l = 10^{-8}$.

values of E_c are not tested. We see that the effectiveness drops for increasing control cost and maximises at $\omega = 0$. Therefore in the following we focus on the steady control perturbation with $\omega = 0$.

The optimal perturbations at $\omega = 0$ are plotted in Fig. 14. To compare the distribution of optimal perturbations at various control costs, the perturbations are normalised so that $[\boldsymbol{c}, \boldsymbol{c}] = 1$. We see that at small values of control cost E_c, the optimal control overlaps with the direct solution as expected. As the control cost increases, the weight of $\boldsymbol{v}_1$ becomes more dominant in the optimal control and therefore results in a more spatially oscillatory profile, similarly as observed in the stenotic flow case (see Fig. 8).

The controlled and uncontrolled evolutions of the optimal initial perturbations are illustrated in Fig. 15, where we see that the transient effect is suppressed significantly by the boundary perturbations. Nonlinear evolution of the controlled and uncontrolled flow is also investigated by DNS of the base flow initially perturbed by the optimal initial perturbation with relative energy level l (ratio between perturbation energy and base flow energy) and plotted in Fig. 15 to compare against the linearised evolution. We see that the optimal control suppresses the transient energy growth significantly in both linearised and nonlinear calculations and the growth in DNS does not reach the optimal growth in the linearised evolution owing to the nonlinear saturation.

The final outcomes of the controlled and uncontrolled flow field in linearised developments are presented in Fig. 16. We see that during the linearised evolution, the perturbations are convected downstream and amplified to form spiral structures. Under the control of optimal boundary perturbations, the magnitude of the spiral structures are significantly weakened.

The control effects and the relevance of the development of perturbations to spiral vortex breakdown are further studied as revealed in Fig. 17. To illustrate the structures of the vortex, we adopt iso-surfaces of the intermediate eigenvalue of the velocity gradient tensor, "λ_2" [31]. We see that without control, the optimal initial perturbations develop into spiral arms, but under the optimal inflow boundary control, the spiral structures are effectively suppressed.

5. Conclusion

An optimisation of boundary control to minimise the energy growth of a given perturbation in the domain is presented in order to underpin the design of feed-back control laws, in terms of choosing the location of actuators and predicting the maximum control effect that can be expected. The optimal initial perturbation and its outcome are adopted as the control objective since the optimal initial perturbation is the most energetic component of a random noise and therefore also the target for feed-back control.

A Lagrangian functional consisting of the controlled transient energy and a constraint on the control cost is built. The gradient of this Lagrangian functional is formulated as an explicit function of the boundary perturbation and a conjugate gradient method is used to calculate the search direction. Owing to the linear nature of the governing equations, an optimal step length exists and can be calculated by an extra integration of the LNS equations. It is analytically presented that at a given control cost, a unique optimal boundary control exists. At small enough control cost, a sensitivity solution can be obtained after a solo integration of the adjoint equations without iterative optimisations. The distribution of this sensitivity solution can be interpreted as the sensitivity of perturbations in the domain on the control. As the control cost increases, this optimal solution approaches the stablest eigenmode of a direct-adjoint operator and tends to be grid-to-grid oscillatory, which cannot be generated by physical actuators.

After optimising the boundary control based on fixed values of control cost, a controllability analysis is conducted by relaxing the constraint on control cost. The obtained "global" optimal control reveals the magnitude and distribution of the uncontrollable component in the objective perturbation.

It is observed that without constraint on control cost, over 95% of the transient energy growth can be suppressed and this value is relatively insensitive to the temporal frequency of the boundary perturbations in the case study of a stenotic flow. In the investigation of another case, the Batchelor vortex, we observe that the spiral breakdown initialised by the helical instabilities are effectively suppressed by the inflow-normal boundary control in DNS.

Acknowledgements

We would like to acknowledge financial support from the Australian Research Council through Discovery Program Grant DP1094851, and from Australia's National Computational Infrastructure via Merit Allocation Scheme Grant D77. SJS would like to acknowledge financial support under EPSRC Grant EP/H050507/1.

Appendix A. Search direction and optimal step length

In the optimisation process, we adopt the (Fletcher–Reeves) conjugate gradient method to calculate the search direction at step k as

$$\tilde{\mathcal{P}}(\nabla_{\boldsymbol{c}}\mathcal{L})^k = (\nabla_{\boldsymbol{c}}\mathcal{L})^k, \qquad \text{for } k = 0;$$

$$\tilde{\mathcal{P}}(\nabla_{\boldsymbol{c}}\mathcal{L})^k = (\nabla_{\boldsymbol{c}}\mathcal{L})^k + \frac{((\nabla_{\boldsymbol{c}}\mathcal{L})^k, (\nabla_{\boldsymbol{c}}\mathcal{L})^k)}{((\nabla_{\boldsymbol{c}}\mathcal{L})^{k-1}, (\nabla_{\boldsymbol{c}}\mathcal{L})^{k-1})}\mathcal{P}(\nabla_{\boldsymbol{c}}\mathcal{L})^{k-1} \quad \text{for } k > 0.$$

The search direction can be decomposed into two parts, one is parallel to $\boldsymbol{c}$ and the other is normal to $\boldsymbol{c}$. The first part does not change

the distribution of $\boldsymbol{c}$ and can be removed. To simplify the formulation in the calculation of the optimal step length outlined below, we use only the second part as the search direction,

$$\mathcal{P}(\nabla_{\boldsymbol{c}}\mathcal{L})^k = \tilde{\mathcal{P}}(\nabla_{\boldsymbol{c}}\mathcal{L})^k - \frac{[\tilde{\mathcal{P}}(\nabla_{\boldsymbol{c}}\mathcal{L})^k, \boldsymbol{c}^k]}{[\boldsymbol{c}^k, \boldsymbol{c}^k]}\boldsymbol{c}^k.$$

The optimal step length α_{opt} is the step length α that minimises

$$E(\boldsymbol{c}^{k+1}) = [2\mathcal{N}^*\boldsymbol{u}_{i\tau} + \mathcal{N}^*\mathcal{N}\boldsymbol{c}^{k+1}, \boldsymbol{c}^{k+1}] + (\boldsymbol{u}_{i\tau}, \boldsymbol{u}_{i\tau})$$

where

$$\boldsymbol{c}^{k+1}(\alpha) = (\boldsymbol{c}^k + \alpha\mathcal{P}^k)\left(\frac{E_c}{[\boldsymbol{c}^k + \alpha\mathcal{P}^k, \boldsymbol{c}^k + \alpha\mathcal{P}^k]}\right)^{1/2}.$$

Therefore E can be expressed as a function of α:

$$E(\boldsymbol{c}^{k+1}(\alpha)) = \frac{(a_6 + a_2\alpha)(1 + a_1\alpha^2)^{1/2} + a_3 + a_4\alpha + a_5\alpha^2}{1 + a_1\alpha^2} + (\boldsymbol{u}_{i\tau}, \boldsymbol{u}_{i\tau}) \tag{A.1}$$

where

$$a_1 = [\mathcal{P}, \mathcal{P}]/E_c, \quad a_2 = 2[\mathcal{N}^*\boldsymbol{u}_{i\tau}, \mathcal{P}], \quad a_3 = (\mathcal{N}\boldsymbol{c}, \mathcal{N}\boldsymbol{c}),$$
$$a_4 = 2(\mathcal{N}\boldsymbol{c}, \mathcal{N}\mathcal{P}), \quad a_5 = (\mathcal{N}\mathcal{P}, \mathcal{N}\mathcal{P}), \quad a_6 = 2[\mathcal{N}^*\boldsymbol{u}_{i\tau}, \boldsymbol{c}].$$

The superscript k is omitted hereafter for clarification.

At the optimal value of α, $\mathrm{d}L/\mathrm{d}\alpha = 0$. Through standard algebraic manipulations, we obtain

$$c_4\alpha^4 + c_3\alpha^3 + c_2\alpha^2 + c_1\alpha + c_0 = 0, \tag{A.2}$$

where

$$c_0 = a_4^2 - a_2^2, \quad c_1 = -4a_1a_3a_4 + 4a_4a_5 + 2a_1a_2a_6,$$
$$c_2 = (2a_1a_3 - 2a_5)^2 - 2a_1a_4^2 - a_1a_2^2 - a_1^2a_6^2,$$
$$c_3 = 2a_1(2a_1a_3a_4 - 2a_4a_5 + a_1a_2a_6), \quad c_4 = a_1^2\left(a_4^2 - a_1a_6^2\right).$$

The roots of (A.2) are the eigenvalues of a Hessenberg matrix

$$C = \begin{bmatrix} 0 & 0 & 0 & -c_0/c_4 \\ 1 & 0 & 0 & -c_1/c_4 \\ 0 & 1 & 0 & -c_2/c_4 \\ 0 & 0 & 1 & -c_3/c_4 \end{bmatrix}.$$

The eigenvalues of C are calculated via Schur factorisation and denoted as $\alpha_1 \sim \alpha_4$. Considering $-\infty$ is also a candidate of the optimal step length, we set $\alpha_5 = -\infty$. Substitute $\alpha_1 \sim \alpha_5$ into (A.1) and compare the corresponding values of E. Then the step length that produces the minimum value of E is the optimal step length α_{opt}.

References

[1] Trefethen LN, Trefethen AE, Reddy SC, Driscoll TA. Hydrodynamic stability without eigenvalues. Science 1993;261:578–84.
[2] Schmid PJ, Henningson DS. Stability and transition in shear flows. Springer; 2001.
[3] Chomaz J-M. Global instabilities in spatially developing flows: non-normality and nonlinearity. Annu Rev Fluid Mech 2005;37:357–92.
[4] Schmid PJ. Nonmodal stability theory. Annu Rev Fluid Mech 2007;39:129–62.
[5] Luchini P, Bottaro A. Adjoint equations in stability analysis. Annu Rev Fluid Mech 2014;46:493–517.
[6] Marquet O, Sipp D, Chomaz JM, Jacquin L. Amplifier and resonator dynamics of a low-Reynolds-number recirculation bubble in a global framework. J Fluid Mech 2008;605:429–43.
[7] Barkley D, Blackburn HM, Sherwin SJ. Direct optimal growth analysis for timesteppers. Int J Numer Methods Fluids 2008;57:1437–58.
[8] Pralits JO, Brandt L, Giannetti F. Instability and sensitivity of the flow around a rotating circular cylinder. J Fluid Mech 2010;650:513–36.
[9] Mao X, Blackburn HM, Sherwin SJ. Optimal inflow boundary condition perturbations in steady stenotic flows. J Fluid Mech 2012;705:306–21.
[10] Sipp D, Marquet O. Characterization of noise amplifiers with global singular modes: the case of the leading-edge flat-plate boundary layer. Theor Comput Fluid Dyn 2013;27:617–35.
[11] Mao X, Blackburn HM, Sherwin SJ. Calculation of global optimal initial and boundary perturbations for the linearised incompressible Navier–Stokes equations. J Comput Phys 2013;235:258–73.
[12] Brandt L, Sipp D, Pralits JO, Marquet O. Effects of base-flow variation in noise amplifiers: the flat-plate boundary layer. J Fluid Mech 2011;687:503–28.
[13] Mao X. Effects of base flow modifications on receptivity and non-normality: flow past a backward-facing step. J Fluid Mech 2015;771:229–63.
[14] Mao X, Blackburn HM, Sherwin SJ. Nonlinear optimal suppression of vortex shedding from a circular cylinder. J Fluid Mech 2015;775:241–65.
[15] Guégan A, Schmid PJ, Huerre P. Optimal energy growth and optimal control in swept Hiemenz flow. J Fluid Mech 2006;566:11–45.
[16] Leclerca E, Sagauta P, Mohammadic B. On the use of incomplete sensitivities for feedback control of laminar vortex shedding. Comput Fluids 2006;35(10):1432–43.
[17] Sipp D, Marquet O, Meliga P, Barbagallo A. Dynamics and control of global instabilities in open flows: a linearized approach. Appl Mech Rev 2010;63:030801.
[18] Hervé A, Sipp D, Schmid P, Samuelides M. A physics-based approach to flow control using system identification. J Fluid Mech 2012;702:26–58.
[19] Dahan J, Morgans A, Lardeau S. Feedback control for form-drag reduction on a bluff body with a blunt trailing edge. J Fluid Mech 2012;704:360–87.
[20] Mao X, Sherwin SJ, Blackburn HM. Transient growth and bypass transition in stenotic flow with a physiological waveform. Theor Comput Fluid Dyn 2011;25(1):31–42.
[21] Blackburn HM, Sherwin SJ, Barkley D. Convective instability and transient growth in steady and pulsatile stenotic flows. J Fluid Mech 2008;607:267–77.
[22] Barkley D, Henderson RD. Three-dimensional Floquet stability analysis of the wake of a circular cylinder. J Fluid Mech 1996;322:215–41.
[23] Blackburn HM, Sherwin SJ. Formulation of a Galerkin spectral element–Fourier method for three-dimensional incompressible flows in cylindrical geometries. J Comput Phys 2004;197(2):759–78.
[24] Karniadakis GE, Israeli M, Orszag SA. High-order splitting methods for the incompressible Navier–Stokes equations. J Comput Phys 1991;97(2):414–43.
[25] Batchelor GK. Axial flow in trailing line vortices. J Fluid Mech 1964;20:645–58.
[26] Lessen M, Singh PJ, Paillet F. The stability of a trailing line vortex. Part 1. Inviscid theory. J Fluid Mech 1974;63:753–63.
[27] Stewartson K, Brown SN. Near-neutral centre-modes as inviscid perturbations to a trailing line vortex. J Fluid Mech 1985;156:387–99.
[28] Heaton CJ. Centre modes in inviscid swirling flows and their application to the stability of the Batchelor vortex. J Fluid Mech 2007;576:325–48.
[29] Broadhurst MS, Sherwin SJ. Helical instability and breakdown of a Batchelor trailing vortex. Math Ind 2008;12:191–5.
[30] Ash RL, Khorrami MR. Vortex stability. Fluid vortices. Green SI, editor. Dorcrecht: Kluwer; 1995.
[31] Jeong J, Hussain F. On the identification of a vortex. J Fluid Mech 1995;285:69–94.